A&A 567, A18 (2014)
DOI: 10.1051/0004-6361/201423729

Astronomy & Astrophysics

Atomic data for astrophysics: Ni XV*

G. Del Zanna[1], P. J. Storey[2], and H. E. Mason[1]

[1] DAMTP, Centre for Mathematical Sciences, Wilberforce Road, Cambridge CB3 0WA, UK
e-mail: g.del-zanna@damtp.cam.ac.uk
[2] Department of Physics and Astronomy, University College London, Gower Street, London WC1E 6BT, UK

Received 28 February 2014 / Accepted 30 April 2014

ABSTRACT

We present the first R-matrix scattering calculation for electron collisional excitation of Ni XV. The large-scale target includes configurations up to $n = 4$. The calculations were carried out using the intermediate-coupling frame transformation method. Significant enhancements in the collision strengths, compared to previous distorted-wave (DW) calculations, are found for several cases, in particular the forbidden lines within the ground configuration and the $3s^2$ 3p 4s levels. We provide a complete set of rates and a list of strongest lines that are observable in astrophysical plasmas. Previous identifications are reviewed, and a few new ones suggested. The new data can be used to accurately measure electron densities for high-temperature (3 MK) plasmas, and the nickel abundance.

Key words. atomic data – line: identification – techniques: spectroscopic – Sun: corona

1. Introduction

Ni XV produces strong decays from the 3s $3p^3$ and $3s^2$ 3p 3d configurations in the extreme ultraviolet (EUV) region of the spectrum (Behring et al. 1972), most of which were identified by Fawcett & Hayes (1972) and Fawcett & Hatter (1980). Some of these lines are useful density and abundance diagnostics for high-temperature (3 MK) plasmas, such as those of solar active region cores (Del Zanna 2013b).

Ni XV also produces two important forbidden lines (within the $n = 3$) in the visible region of the spectrum, identified by Edlén (1942), and often observed during total solar eclipses (e.g. Aly et al. 1962; Jefferies et al. 1971; Fisher & Pope 1971; Mason 1973). They are also potentially very useful density diagnostics, like the well known isoelectronic Fe XIII infrared lines. Ni XV soft X-ray transitions from the $n = 4$ levels have also been observed in the laboratory (Fawcett et al. 1972; Kastner et al. 1978).

Landi & Bhatia (2012) published the first complete scattering calculation for this ion. They used the Flexible Atomic Code (Gu 2004) and the distorted-wave (DW) approximation to calculate collision strengths to the $3s^2$ $3p^2$, 3s $3p^3$, $3s^2$ 3p 3d, $3p^4$, 3s $3p^2$ 3d, and $3s^2$ 3p 4l (l = s, p, d, f) configurations.

Ni XV is isoelectronic with Fe XIII, for which we now have a fairly complete set of line identifications and atomic data. A complete review of the Fe XIII line identifications and wavelengths for the $n = 3$ levels was given in Del Zanna (2011), where a number of new energy levels were identified, using the Iron Project scattering calculations of Storey & Zeippen (2010). These authors performed an R-matrix calculation for the lowest 54 LS terms and 114 fine-structure levels within the $n = 3$ complex.

In Del Zanna & Storey (2013) we carried out a large-scale R-matrix (up to $n = 4$) scattering calculations for electron collisional excitation of Fe XIII. For the scattering close-coupling calculation, we retained 749 fine-structure levels arising from the first 331 LS terms. As found in previous similar work on Fe X (Del Zanna et al. 2012), the excitation rates to some of the states of the $n = 4$ configurations are significantly increased by resonances converging on other $n = 4$ states.

Our experience on the Fe XIII shows that the DW approximation significantly underestimates the collisions strengths, especially for the energetically lowest configurations. An R-matrix calculation for this ion was therefore needed, to improve on the Landi & Bhatia (2012) calculations. In Sect. 2 we outline the methods we adopted for the scattering calculations. In Sect. 3 we present our results and in Sect. 4 we reach our conclusions.

2. Methods

The atomic structure calculations were carried out using the AUTOSTRUCTURE program (Badnell 2011), which originated from the SUPERSTRUCTURE program (Eissner et al. 1974). AUTOSTRUCTURE constructs target wavefunctions using radial wavefunctions calculated in a scaled Thomas-Fermi-Dirac statistical model potential with a set of scaling parameters. The program also provides radiative rates and infinite energy Born limits. These limits are particularly important from two aspects. First, they allow a consistency check of the collision strengths in the scaled Burgess & Tully (1992) domain (see also Burgess et al. 1997). Second, they are used in the interpolation of the collision strengths at high energies.

The R-matrix method used in the scattering calculation is described in Hummer et al. (1993) and Berrington et al. (1995). We performed the calculation in the inner region in LS coupling and included mass and Darwin relativistic energy corrections.

The outer region calculation used the intermediate-coupling frame transformation method (ICFT) described by Griffin et al. (1998), in which the transformation of the multi-channel

* The full dataset (energies, transition probabilities and rates) is available from our APAP website http://www.apap-network.org, and also at the CDS via anonymous ftp to cdsarc.u-strasbg.fr (130.79.128.5) or via http://cdsarc.u-strasbg.fr/viz-bin/qcat?J/A+A/567/A18

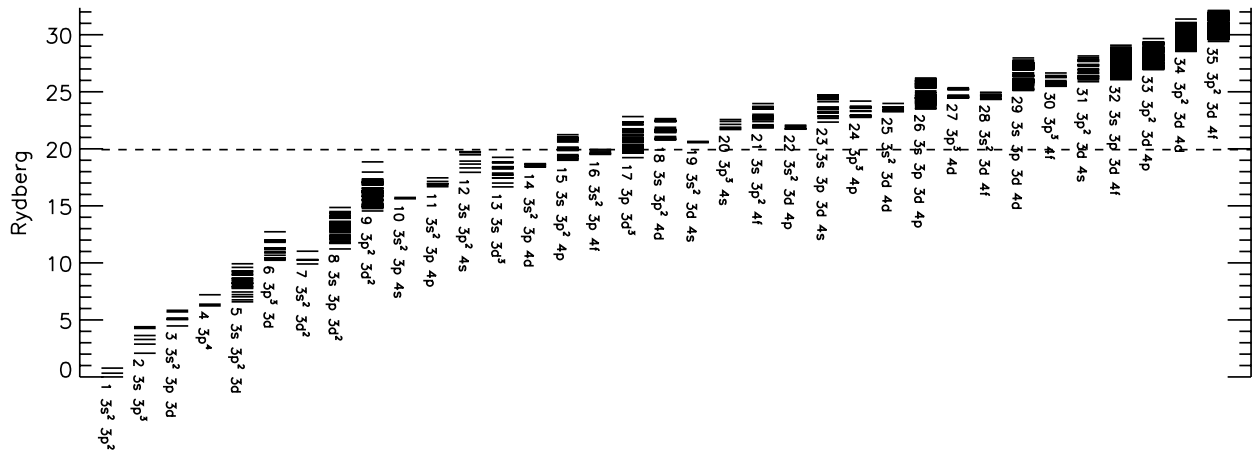

Fig. 1. Term energies of the target levels. The lowest 230 terms which produce levels having energies below the dashed line have been retained for the close-coupling expansion.

quantum defect theory unphysical K-matrix to intermediate coupling uses the so-called term-coupling coefficients (TCCs) in conjunction with level energies.

Dipole-allowed transitions were topped-up to infinite partial wave using an intermediate coupling version of the Coulomb-Bethe method as described by Burgess (1974) while non-dipole-allowed transitions were topped up assuming that the collision strengths form a geometric progression in J (see Badnell & Griffin 2001).

The collision strengths were extended to high energies by interpolation using the appropriate high-energy limits in the Burgess & Tully (1992) scaled domain. The high-energy limits were calculated with AUTOSTRUCTURE for both optically-allowed (see Burgess et al. 1997) and non-dipole-allowed transitions (see Chidichimo et al. 2003).

We have also carried out Breit-Pauli DW calculations using the recent development of the AUTOSTRUCTURE code, described in detail in Badnell (2011).

The temperature-dependent effective collisions strength $\Upsilon(i-j)$ were calculated by assuming a Maxwellian electron distribution and linear integration with the final energy of the colliding electron.

Table 1. Target electron configuration basis and orbital scaling parameters λ_{nl}.

Configurations	Orbital	λ_{nl}
$3s^2\ 3p^2$	1s	1.40365
$3s^2\ 3p\ 3d$	2s	1.11531
$3s^2\ 3p\ 4l$ (l = s, p, d, f)	2p	1.05961
$3s^2\ 3d\ 4l$ (l = s, p, d, f)	3s	1.12141
$3s^2\ 3d^2$	3p	1.09030
$3s\ 3p^3$	3d	1.10852
$3s\ 3p^2\ 3d$	4s	1.14489
$3s\ 3p^2\ 4l$ (l = s, p, d, f)	4p	1.11294
$3s\ 3p\ 3d^2$	4d	1.13787
$3s\ 3p\ 3d\ 4l$ (l = s, p, d, f)	4f	1.27710
$3s\ 3d^3$		
$3p^4$		
$3p^3\ 3d$		
$3p^3\ 4l$ (l = s, p, d, f)		
$3p^2\ 3d^2$		
$3p^2\ 3d\ 4l$ (l = s, p, d, f)		
$3p\ 3d^3$		

3. Results

3.1. The scattering calculation

For our configuration basis we have chosen the complete set of 35 $n = 3, 4$ configurations shown in Fig. 1 and listed in Table 1. They give rise to 944 LS terms and 2186 fine-structure levels. The scaling parameters λ_{nl} for the potentials in which the orbital functions are calculated are also given in Table 1.

In our $n = 4$ calculations for Fe XIII (Del Zanna & Storey 2013), we found very small differences in the collision strengths to the $n = 3$ levels, compared to the previous results of Storey & Zeippen (2010). This means that the main resonances affecting the $n = 3$ levels are from within the $n = 3$ complex. Since in this paper we are primarily interested in the $n = 3$ diagnostics, we have chosen for the close-coupling expansion of Ni XV a set of LS terms that is slightly reduced, compared to what we adopted for Fe XIII. The 483 fine-structure levels arising from the (energetically) lowest 230 LS terms were retained for the scattering calculation. They include all the spectroscopically important levels, up to $n = 4$, in particular those from the $3s^2\ 3p\ 4l$ (l = s, p, d, f) configurations.

Table 2 presents a selection of fine-structure target level energies E_t, compared to experimental energies E_{exp}. The experimental energies are mostly taken from the NIST compilation (Kramida et al. 2013), which in turn relied on the identifications mentioned in the introduction. We also suggest some new identifications, as described below.

We note that the level $3s^2\ 3p^2\ ^1S_0$ is not listed by NIST, but was identified by Feldman et al. (1998) from the 2–5 $3s^2\ 3p^2\ ^3P_1$–$3s^2\ 3p^2\ ^1S_0$ transition observed by SOHO SUMER at 1033.04 Å. A few $3s\ 3p^3$ levels were in principle identified by Trigueiros et al. (2006) (and also adopted by Landi & Bhatia 2012), however, a close inspection of their results (Table 2) shows a few problems. The energy suggested for the $^3D_3$ (level 9), 335 562 cm^{-1}, is at odds with the NIST one and those of the $^3D_1$ and $^3D_2$, so must be incorrect. The suggested energy for the $^3P_0$ (level 10), 385 082 cm^{-1}, is at odds with the energy of the $^3P_2$, so it must also be incorrect. The energy of the $^3P_2$ was listed as new, but was actually obtained by Fawcett & Hayes (1972). The only new energy listed by Trigueiros et al. (2006) that is correct is that of the $^3P_1$ (level 11). Its value can be estimated quite accurately from the energy of the $^3P_2$, and it is

Table 2. Level energies for Ni XV.

i	Conf.	Mixing	Lev.	E_{exp}	E_t	
1	$3s^2\ 3p^2$	(91%)	$^3P_0$	0.0	0.0	
2	$3s^2\ 3p^2$	(96%)	$^3P_1$	14 917.5	14 319.0 (599)	
3	$3s^2\ 3p^2$	(84%) +4(12%)	$^3P_2$	27 376.5	27 010.0 (367)	
4	$3s^2\ 3p^2$	(84%) +3(12%)	$^1D_2$	62 852.1	63 770.0 (–918)	
5	$3s^2\ 3p^2$	(90%)	$^1S_0$	111 719.0	113 903.0 (–2184)	F98
6	$3s\ 3p^3$	(97%)	$^5S_2$	254 700.0	248 965.0 (5735)	
7	$3s\ 3p^3$	(82%) +23(c3 10%)	$^3D_1$	335 400.0	333 779.0 (1621)	
8	$3s\ 3p^3$	(80%) +25(c3 9%) +12(6%)	$^3D_2$	335 682.0	334 081.0 (1601)	
9	$3s\ 3p^3$	(87%) +24(c3 10%)	$^3D_3$	340 794.0	339 070.0 (1724)	
10	$3s\ 3p^3$	(88%) +22(c3 8%)	$^3P_0$	–	383 767.0	
11	$3s\ 3p^3$	(83%) +20(c3 8%)	$^3P_1$	385 460.0	385 158.0 (302)	T06
12	$3s\ 3p^3$	(72%) +8(6%) +13(5%) +19(c3 8%)	$^3P_2$	386 590.0	386 249.0 (341)	
13	$3s\ 3p^3$	(50%) +21(c3 37%) +12(7%)	$^1D_2$	422 855.0	424 254.0 (–1399)	
14	$3s\ 3p^3$	(72%) +17(20%)	$^3S_1$	478 041.0	483 279.0 (–5238)	
15	$3s^2\ 3p\ 3d$	(95%)	$^3F_2$	–	498 912.0	
16	$3s^2\ 3p\ 3d$	(95%)	$^3F_3$	–	508 965.0	
17	$3s\ 3p^3$	(65%) +27(c3 8%) +14(22%)	$^1P_1$	509 167.0	514 636.0 (–5469)	
18	$3s^2\ 3p\ 3d$	(97%)	$^3F_4$	–	524 073.0	
19	$3s^2\ 3p\ 3d$	(45%) +25(9%) +13(c2 15%) +21(20%)	$^3P_2$	555 797.0	564 331.0 (–8534)	
20	$3s^2\ 3p\ 3d$	(46%) +23(38%)	$^3P_1$	565 800.0	574 026.0 (–8226)	
21	$3s^2\ 3p\ 3d$	(33%) +25(17%) +13(c2 21%) +19(17%)	$^1D_2$	574 267.0	582 273.0 (–8006)	
22	$3s^2\ 3p\ 3d$	(87%) +10(c2 8%)	$^3P_0$	–	584 562.0	
23	$3s^2\ 3p\ 3d$	(45%) +7(c2 6%) +20(39%)	$^3D_1$	582 760.0	590 380.0 (–7620)	
24	$3s^2\ 3p\ 3d$	(84%) +9(c2 9%)	$^3D_3$	585 185.0	594 064.0 (–8879)	
25	$3s^2\ 3p\ 3d$	(58%) +8(c2 7%) +19(23%)	$^3D_2$	586 379.0	594 578.0 (–8199)	
26	$3s^2\ 3p\ 3d$	(94%)	$^1F_3$	638 477.0	650 236.0 (–11 759)	
27	$3s^2\ 3p\ 3d$	(84%) +17(c2 8%)	$^1P_1$	–	666 242.0	
279	$3s^2\ 3p\ 4s$	(95%)	$^3P_2$	1 730 700.0	1 745 611.0 (–14 911)	
283	$3s^2\ 3p\ 4s$	(79%) +271(15%)	$^1P_1$	1 741 300.0	1 755 249.0 (–13 949)	
328	$3s^2\ 3p\ 4p$	(87%)	$^3P_0$	1 852 850.0	1 867 519.0 (–14 668)	TN
376	$3s\ 3p^2\ 4s$	(92%)	$^3P_0$	2 013 534.0	2 018 280.0 (–4746)	N
385	$3s^2\ 3p\ 4d$	(60%) +392(22%) +395(10%)	$^3D_2$	2 018 400.0	2 037 045.0 (–18 645)	
389	$3s^2\ 3p\ 4d$	(46%) +393(33%) +398(13%)	$^3D_3$	2 020 500.0	2 039 984.0 (–19 484)	
393	$3s^2\ 3p\ 4d$	(46%) +389(45%)	$^3F_3$	2 042 500.0	2 059 762.0 (–17 262)	
398	$3s^2\ 3p\ 4d$	(77%) +393(14%)	$^1F_3$	2 053 000.0	2 071 507.0 (–18 507)	
439	$3s^2\ 3p\ 4f$	(79%) +466(10%) +484(5%)	$^3F_2$	2 138 869.0	2 164 303.0 (–25 433)	TN
482	$3s^2\ 3p\ 4f$	(90%)	$^1G_4$	2 185 600.0 ± –1	2 212 351.0 (–26 751)	

Notes. The first column indicates the (unique) level index, and the second the configuration. The third column indicates the mixing of the levels. For example, level No. 3 is due by 84% to the $^3P_2$ and by 12% to the $^1D_2$ (level No. 4). Level No. 7 is due by 82% to the $3s\ 3p^3\ ^3D_1$ and by 10% to level No. 23 (from the third configuration in energy order, the $3s^2\ 3p\ 3d$), the $^3D_1$. Only the main contributing terms (above 10%) are listed. The fourth column indicates the dominant $LS\,J$ contribution to the level. The experimental level energies E_{exp} (cm^{-1}) are shown in Col. 5 while Col. 6 lists those obtained from our scattering target E_t. Values in parentheses indicate differences with E_{exp}. Only a selection of levels is shown, the lowest 27 and the few with known experimental energies. The experimental energies are from the NIST compilation, with a few exceptions: F98: Feldman et al. (1998); T06: Trigueiros et al. (2006), confirmed here; N indicates a level with a new experimental energy, and TN with a tentative new one.

in agreement with the wavelength of the $3s^2\ 3p^2\ ^3P_0$–$3s\ 3p^3\ ^3P_1$ line, observed at 259.43 Å by Trigueiros et al. (2006). We can confirm independently this identification because we observe the $3s^2\ 3p^2\ ^3P_1$–$3s\ 3p^3\ ^3P_1$ line with Hinode EIS at 269.87 Å (see Del Zanna 2012b). The energies of the few $n = 4$ levels are discussed below.

A set of "best" energies E_b was obtained with a linear fit between the E_{exp} and E_t values. The E_b values were used (whenever the experimental energies E_{exp} were not available) within the R-matrix calculation to obtain a better position of the resonance thresholds. The experimental energies E_{exp} and the "best" energies E_b were also used to calculate the transition probabilities, which was done with a separate AUTOSTRUCTURE calculation.

The expansion of each scattered electron partial wave was done over a basis of 18 functions within the R-matrix boundary and the partial wave expansion extended to a maximum total orbital angular momentum quantum number of $L = 16$. This produces reliable collision strengths up to about 80 Ryd.

The outer region calculation includes exchange up to a total angular momentum quantum number $J = 27/2$. We have supplemented the exchange contributions with a non-exchange calculation extending from $J = 29/2$ to $J = 75/2$. The outer region exchange calculation was performed in a number of stages. A coarse energy mesh was chosen above all resonances. The resonance region itself was calculated with 6400 points.

We calculated the thermally-averaged collision strengths, Υ, which are, as we expected, significantly enhanced compared to

the DW results of Landi & Bhatia (2012), for several important transitions. A few examples are given in Fig. 2. The enhancements mainly affect the transitions between levels of the ground configuration. For strong dipole-allowed transitions the effects of the resonances are expected to be small, and indeed we find excellent agreement between our thermally averaged collision strengths and those of Landi & Bhatia (2012), as illustrated by the 1–14 and 1–20 transitions in Fig. 2.

3.2. Comparison to observations

We have constructed an ion population model with the new R-matrix collision strengths, complemented with a set of A-values calculated separately with exactly the same configuration basis as the scattering target, but with the experimental and best energies. We then calculated line intensities and looked at how levels are populated at $\log N_e$ [cm^{-3}] = 9 (a typical solar active region density) and $\log T_e$ [K] = 6.4, the temperature of maximum ion abundance for Ni XV in ionization equilibrium. The brightest lines are listed in Table 3.

The strongest EUV line, at 176.74 Å, is well visible with the Hinode EIS instrument, and indeed has been used e.g. in Del Zanna (2013b) to measure the nickel abundance in hot active region loops, relative to other elements. This line, in quiet Sun coronal observations, is blended with an Fe VII line (Del Zanna 2009).

The density-sensitive line at 179.27 Å (which is actually a self-blend with a weaker transition) is very close in wavelength to the strongest line at 176.74 Å. These two lines are therefore an excellent density diagnostic, like the widely used Fe XIII 202, 203.8 Å lines. One problem is that these lines fall in a spectral region where the Hinode EIS sensitivity decreases very rapidly, hence long exposures are needed. We use here a spectrum of an active region core, observed on 2010 October 26, and discussed in Del Zanna (2013b). Parts of this spectrum are shown in Fig. 3.

The other Ni XV EUV lines observed by EIS are difficult to observe because they fall very close to other lines. The 184.88 Å is measurable, but it is in the red wing of a strong Fe XI line. The 185.69 Å line is blended with an unidentified line, and the 189.24 Å is also in the red wing of a much stronger line (for a discussion on identifications of EIS coronal lines see Del Zanna 2009, 2012b).

We use the new in-flight EIS radiometric calibration described in Del Zanna (2013a). This has significant differences compared to the ground calibration.

We show in Fig. 4 the "emissivity ratio" curve

$$F_{ji} = \frac{I_{ob} N_e}{N_j(N_e, T_e)\, A_{ji}}\, C \qquad (1)$$

for each line as a function of the electron density N_e. I_{ob} is the observed intensity of the line, $N_j(N_e, T_e)$ is the population of the upper level j relative to the total number density of the ion, calculated at a fixed temperature T_e. A_{ji} is the spontaneous radiative transition probability, and C is a scaling constant. This constant is the same for all the lines, and its value is 1.25×10^{10}. This value was chosen so that the emissivity ratios are near unity, to visually estimate, from the spread in the curves, the relative agreement between observed and predicted intensities for all the lines. In fact, if agreement between experimental and theoretical intensities is present, all lines should be closely spaced. If the plasma is nearly isodensity, all curves should cross at one point, giving the line-of-sight averaged density. The emissivity ratio curves are useful to see at once the density sensitivity of

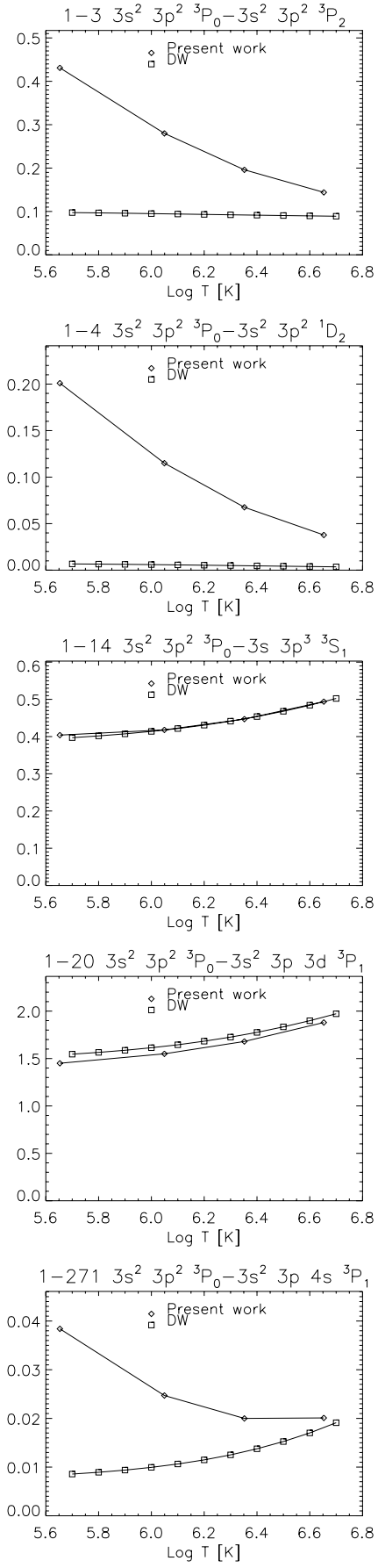

Fig. 2. Thermally averaged collision strengths for a selection of transitions (see text). The DW results are from Landi & Bhatia (2012).

Table 3. List of the strongest Ni XV lines.

i–j	Levels	I	I	gf	A_{ji}(s^{-1})	λ_{exp}(Å)	λ_{th}(Å)	
			CHIANTI					
1–20	$3s^2\ 3p^2\ ^3P_0$–$3s^2\ 3p\ 3d\ ^3P_1$	1.0	1.0	0.83	5.9×10^{10}	176.741	174.21 (–2.5)	
1–7	$3s^2\ 3p^2\ ^3P_0$–$3s\ 3p^3\ ^3D_1$	0.28	0.25	7.7×10^{-2}	1.9×10^{9}	298.151	299.60 (1.4)	
3–14	$3s^2\ 3p^2\ ^3P_2$–$3s\ 3p^3\ ^3S_1$	0.26	0.23	0.90	4.1×10^{10}	221.895	219.17 (–2.7)	
3–24	$3s^2\ 3p^2\ ^3P_2$–$3s^2\ 3p\ 3d\ ^3D_3$	0.16	0.11	2.50	7.4×10^{10}	179.273	176.35 (–2.9)	
2–14	$3s^2\ 3p^2\ ^3P_1$–$3s\ 3p^3\ ^3S_1$	0.12	0.11	0.41	2.0×10^{10}	215.925	213.24 (–2.7)	
2–23	$3s^2\ 3p^2\ ^3P_1$–$3s^2\ 3p\ 3d\ ^3D_1$	0.10	9.3×10^{-2}	0.64	4.6×10^{10}	176.105	173.59 (–2.5)	
3–20	$3s^2\ 3p^2\ ^3P_2$–$3s^2\ 3p\ 3d\ ^3P_1$	9.9×10^{-2}	0.10	9.1×10^{-2}	5.8×10^{9}	185.727	182.81 (–2.9)	
2–11	$3s^2\ 3p^2\ ^3P_1$–$3s\ 3p^3\ ^3P_1$	8.8×10^{-2}	7.5×10^{-2}	9.2×10^{-2}	2.8×10^{9}	269.87	269.66 (–0.2)	N
3–12	$3s^2\ 3p^2\ ^3P_2$–$3s\ 3p^3\ ^3P_2$	6.2×10^{-2}	3.3×10^{-2}	0.26	4.4×10^{9}	278.386	278.37 (–0.0)	
1–14	$3s^2\ 3p^2\ ^3P_0$–$3s\ 3p^3\ ^3S_1$	5.4×10^{-2}	4.8×10^{-2}	0.17	8.6×10^{9}	209.187	206.92 (–2.3)	
1–11	$3s^2\ 3p^2\ ^3P_0$–$3s\ 3p^3\ ^3P_1$	5.1×10^{-2}	4.3×10^{-2}	4.9×10^{-2}	1.6×10^{9}	–	259.63	
3–16	$3s^2\ 3p^2\ ^3P_2$–$3s^2\ 3p\ 3d\ ^3F_3$	4.9×10^{-2}	2.9×10^{-2}	2.7×10^{-2}	5.8×10^{8}	–	207.49	
3–25	$3s^2\ 3p^2\ ^3P_2$–$3s^2\ 3p\ 3d\ ^3D_2$	5.0×10^{-2}	3.5×10^{-2}	0.89	3.7×10^{10}	178.890	176.19 (–2.7)	
4–17	$3s^2\ 3p^2\ ^1D_2$–$3s\ 3p^3\ ^1P_1$	4.4×10^{-2}	3.9×10^{-2}	0.83	3.7×10^{10}	224.057	221.79 (–2.3)	
2–19	$3s^2\ 3p^2\ ^3P_1$–$3s^2\ 3p\ 3d\ ^3P_2$	4.2×10^{-2}	3.4×10^{-2}	0.62	2.4×10^{10}	184.884	181.81 (–3.1)	
4–21	$3s^2\ 3p^2\ ^1D_2$–$3s^2\ 3p\ 3d\ ^1D_2$	4.0×10^{-2}	2.4×10^{-2}	1.15	4.0×10^{10}	195.536	192.86 (–2.7)	
3–19	$3s^2\ 3p^2\ ^3P_2$–$3s^2\ 3p\ 3d\ ^3P_2$	3.7×10^{-2}	2.7×10^{-2}	0.58	2.2×10^{10}	189.243	186.11 (–3.1)	
2–8	$3s^2\ 3p^2\ ^3P_1$–$3s\ 3p^3\ ^3D_2$	0.11	6.8×10^{-2}	0.15	2.0×10^{9}	311.755	312.73 (1.0)	
3–9	$3s^2\ 3p^2\ ^3P_2$–$3s\ 3p^3\ ^3D_3$	8.9×10^{-2}	5.0×10^{-2}	0.17	1.6×10^{9}	319.063	320.45 (1.4)	
2–7	$3s^2\ 3p^2\ ^3P_1$–$3s\ 3p^3\ ^3D_1$	5.3×10^{-2}	4.4×10^{-2}	1.6×10^{-2}	3.5×10^{8}	312.030	313.03 (1.0)	
1–2	$3s^2\ 3p^2\ ^3P_0$–$3s^2\ 3p^2\ ^3P_1$	1.4	1.0	–	57.	6703.54	6983.71 (280)	
2–3	$3s^2\ 3p^2\ ^3P_1$–$3s^2\ 3p^2\ ^3P_2$	0.81	0.61	–	23.	8026.33	7879.71 (–147)	
3–4	$3s^2\ 3p^2\ ^3P_2$–$3s^2\ 3p^2\ ^1D_2$	0.18	9.8×10^{-2}	–	2.0×10^{2}	2818.84	2720.34 (–98.5)	
2–4	$3s^2\ 3p^2\ ^3P_1$–$3s^2\ 3p^2\ ^1D_2$	0.17	9.1×10^{-2}	–	1.9×10^{2}	2086.18	2022.21 (–64.0)	
2–5	$3s^2\ 3p^2\ ^3P_1$–$3s^2\ 3p^2\ ^1S_0$	4.5×10^{-2}	2.1×10^{-2}	–	2.6×10^{3}	1033.04	1004.17 (–28.9)	
7–376	$3s\ 3p^3\ ^3D_1$–$3s\ 3p^2\ 4s\ ^3P_0$	1.6×10^{-2}	–	0.12	2.3×10^{11}	59.59	59.37 (–0.2)	N (bl)
20–439	$3s^2\ 3p\ 3d\ ^3P_1$–$3s^2\ 3p\ 4f\ ^3F_2$	1.2×10^{-2}	1.3×10^{-2}	1.63	5.4×10^{11}	63.57	62.88 (–0.7)	TN
7–328	$3s\ 3p^3\ ^3D_1$–$3s^2\ 3p\ 4p\ ^3P_0$	1.0×10^{-2}	1.3×10^{-2}	3.1×10^{-2}	4.7×10^{10}	65.90	65.20 (–0.7)	TN
20–328	$3s^2\ 3p\ 3d\ ^3P_1$–$3s^2\ 3p\ 4p\ ^3P_0$	8.1×10^{-3}	1.1×10^{-2}	3.5×10^{-2}	3.8×10^{10}	77.73	77.31 (–0.4)	TN
1–383	$3s^2\ 3p^2\ ^3P_0$–$3s^2\ 3p\ 4d\ ^3D_1$	7.5×10^{-3}	7.9×10^{-3}	0.45	4.1×10^{11}	49.58?	49.11 (–0.5)	
3–271	$3s^2\ 3p^2\ ^3P_2$–$3s^2\ 3p\ 4s\ ^3P_1$	4.5×10^{-3}	2.7×10^{-3}	0.20	1.3×10^{11}	–	58.94	
23–439	$3s^2\ 3p\ 3d\ ^3D_1$–$3s^2\ 3p\ 4f\ ^3F_2$	3.6×10^{-3}	3.9×10^{-3}	0.52	1.7×10^{11}	–	63.53	
3–389	$3s^2\ 3p^2\ ^3P_2$–$3s^2\ 3p\ 4d\ ^3D_3$	3.1×10^{-3}	3.1×10^{-3}	1.04	3.9×10^{11}	50.173	49.68 (–0.5)	
16–327	$3s^2\ 3p\ 3d\ ^3F_3$–$3s^2\ 3p\ 4p\ ^3D_2$	3.1×10^{-3}	3.3×10^{-3}	0.25	6.1×10^{10}	–	74.11	
11–376	$3s\ 3p^3\ ^3P_1$–$3s\ 3p^2\ 4s\ ^3P_0$	2.8×10^{-3}	–	2.3×10^{-2}	4.1×10^{10}	–	61.23	
2–383	$3s^2\ 3p^2\ ^3P_1$–$3s^2\ 3p\ 4d\ ^3D_1$	2.8×10^{-3}	2.8×10^{-3}	0.17	1.5×10^{11}	–	49.45	
7–439	$3s\ 3p^3\ ^3D_1$–$3s^2\ 3p\ 4f\ ^3F_2$	2.6×10^{-3}	2.9×10^{-3}	0.28	1.2×10^{11}	–	54.63	
1–271	$3s^2\ 3p^2\ ^3P_0$–$3s^2\ 3p\ 4s\ ^3P_1$	2.4×10^{-3}	1.5×10^{-3}	0.11	6.9×10^{10}	–	58.02	
14–436	$3s\ 3p^3\ ^3S_1$–$3s\ 3p^2\ 4s\ ^3P_0$	2.3×10^{-3}	–	7.0×10^{-2}	1.3×10^{11}	–	59.56	
20–376	$3s^2\ 3p\ 3d\ ^3P_1$–$3s\ 3p^2\ 4s\ ^3P_0$	2.3×10^{-3}	–	2.5×10^{-2}	3.4×10^{10}	–	69.24	
16–435	$3s^2\ 3p\ 3d\ ^3F_3$–$3s^2\ 3p\ 4f\ ^3G_4$	2.4×10^{-3}	2.3×10^{-3}	3.80	7.6×10^{11}	61.152	60.49 (–0.7)	
8–378	$3s\ 3p^3\ ^3D_2$–$3s\ 3p^2\ 4s\ ^3P_1$	1.9×10^{-3}	–	0.30	1.9×10^{11}	–	59.08	
9–388	$3s\ 3p^3\ ^3D_3$–$3s\ 3p^2\ 4s\ ^3P_2$	2.2×10^{-3}	–	0.44	1.7×10^{11}	–	58.83	
15–439	$3s^2\ 3p\ 3d\ ^3F_2$–$3s^2\ 3p\ 4f\ ^3F_2$	1.9×10^{-3}	2.0×10^{-3}	0.24	8.7×10^{10}	–	60.05	
2–385	$3s^2\ 3p^2\ ^3P_1$–$3s^2\ 3p\ 4d\ ^3D_2$	1.8×10^{-3}	1.3×10^{-3}	0.73	3.9×10^{11}	49.913	49.44 (–0.5)	
2–271	$3s^2\ 3p^2\ ^3P_1$–$3s^2\ 3p\ 4s\ ^3P_1$	1.7×10^{-3}	1.0×10^{-3}	7.7×10^{-2}	4.9×10^{10}	–	58.51	
3–279	$3s^2\ 3p^2\ ^3P_2$–$3s^2\ 3p\ 4s\ ^3P_2$	1.6×10^{-3}	6.2×10^{-4}	0.39	1.5×10^{11}	58.709	58.19 (–0.5)	

Notes. The first and second columns indicate the level indices and spectroscopic notation. Columns 3, 4, show the intensities Int = $N_j A_{ji}/N_e$ (photons) relative to the strongest transition (in the EUV), displayed in decreasing order of intensity. The intensities were calculated at $\log N_e$ [cm^{-3}] = 9 and $\log T_e$ [K] = 6.4, with the present and the CHIANTI v.7 data, which are from Landi & Bhatia (2012). Columns 5 and 6 display the weighted oscillator strength (gf) and the spontaneous radiative transition probability. The last two columns show the wavelengths (in vacuum) corresponding to the experimental and target energies. Values in parentheses list the corresponding wavelength difference. N: new identification, TN: a tentative one.

the different emission lines, but are equivalent to the usual single line ratio plots, where the theoretical ratio of two emission lines is plotted as a function of density. The emissivity ratio curves in Fig. 4 are calculated at $\log T_e$[K] = 6.4, the temperature of maximum ion abundance in ionization equilibrium, i.e. the temperature where, in normal coronal conditions, the Ni XV lines are formed.

Figure 4 shows an excellent agreement between predicted and observed intensities for all the lines, providing a density of about $\log N_e$ = 9.5, typical of active region cores, with the exception of the 269.87, which is brighter than predicted. There is also a small (20%) discrepancy in a branching ratio, between the 2–19 (line No. 4) and the 3–19 (line No. 5). However, these two lines are weak and close to stronger lines (cf. Fig. 3), so their

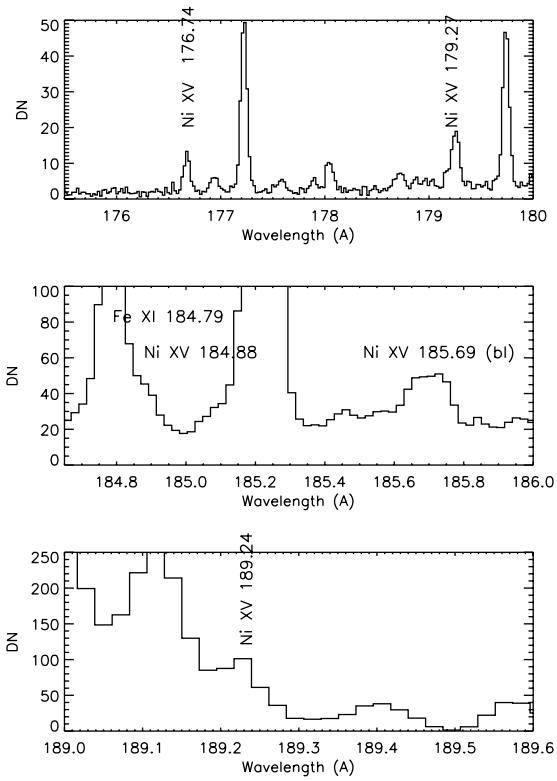

Fig. 3. Hinode EIS spectrum of a hot active region core at the wavelengths where some of the main EUV Ni XV lines are observed.

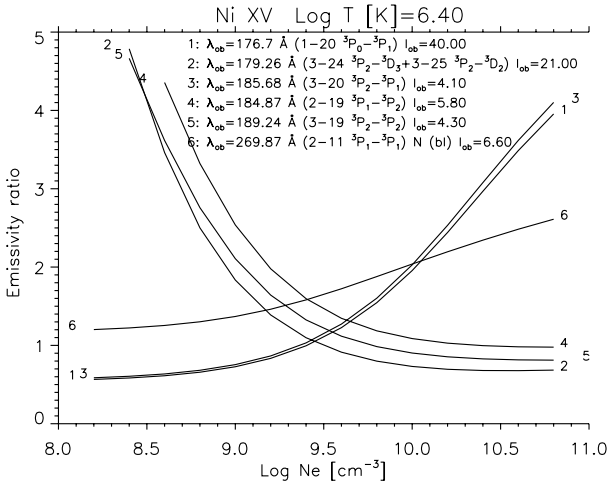

Fig. 4. Emissivity ratio curves for the lines observed by Hinode EIS in a hot active region core. The intensities I_{ob} are in phot cm^{-2} s^{-1} arcsec^{-2}.

observed intensity is difficult to estimate accurately. Finally, we point out that Ni XV has various other density diagnostics in the EUV (not observed by Hinode EIS), such as the 311.8 (strongly blended) and 298.1 Å lines, as discussed by Landi & Bhatia (2012).

3.2.1. Optical forbidden lines

Ni XV also produces several forbidden lines in the UV and visible part of the spectrum, as shown in Table 3.

The main visible forbidden lines are observed at 6702 and 8024 Å (air wavelengths), and are excellent density diagnostics, although they are significantly affected by photoexcitation, as

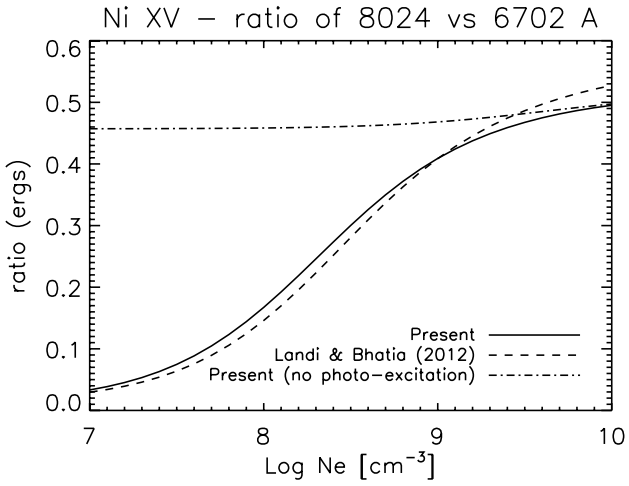

Fig. 5. Theoretical ratio of the main two visible forbidden lines from Ni XV, without photoexcitation (dot-dashed line) and with photoexcitation included, for a distance of 1.03 solar radii from Sun centre and a black-body photospheric spectrum at 6000 K.

already pointed out by Landi & Bhatia (2012), and as shown in Fig. 5. Clearly, any density measurement from these lines needs to take carefully into account photoexcitation and line-of-sight integration. The quiet Sun eclipse measurements of Fisher & Pope (1971) are consistent with an electron density of log Ne [cm^{-3}] = 8, slightly lower than the density obtained from the stronger Fe XIII forbidden lines (log Ne [cm^{-3}] = 8.4), which were observed simultaneously. The difference in electron density might be real, considering that Ni XV is formed at higher temperatures than Fe XIII.

It is interesting to notice the relatively small difference in the ratio of these two lines, compared to the ratio calculated with the DW rates from Landi & Bhatia (2012), despite the large differences in the collision strengths from the ground state, between the DW and the R-matrix calculations. This occurs because the levels of the ground configuration are mainly populated by cascading.

3.2.2. The soft X-ray lines

As in the case of the iron ions, soft X-ray transitions for Ni XV were identified in the laboratory, mostly by B.C. Fawcett. In Fawcett et al. (1972), he identified a few lines originating from the 3s^2 3p 4s, 3s^2 3p 4d, and 3s^2 3p 4f. Later, Kastner et al. (1978) identified a few more decays from the 3s^2 3p 4d, and 3s^2 3p 4f configurations, although most of them had question marks. As in the case of Fe XIII and the other iron ions, the strongest soft X-ray transitions for Ni XV in typical solar/astrophysical conditions were not identified/observed in the laboratory, as shown in Table 3. The relative differences between observed and predicted wavelengths for the few known transitions is very small, so we can predict the wavelengths of the unidentified transitions quite accurately.

The Ni XV soft X-ray lines are intrinsically weaker than the iron lines, so only the few brightest ones should be observable. The brightest is a decay from a core-excited state, the 7–376 3s 3p^3 ^{3}D$_1$–3s 3p^2 4s ^{3}P$_0$ transition. We identified these types of transitions for the first time for Fe X in Del Zanna et al. (2012) and for Fe XI, Fe XII, Fe XIII, and Fe XIV in Del Zanna (2012a), using an excellent soft X-ray spectrum obtained during an M1-class flare from a sounding rocket flight (Acton et al. 1985, hereafter A85). The spectral resolution was

excellent, clearly resolving lines only 0.04 Å apart. The radiometric calibration was also very good. The predicted wavelength of the 7–376 line is 59.37 Å. There is a strong line at 59.59 Å in the A85 spectrum, and listed as a blend. The benchmark of the Fe XIV soft X-ray lines showed that less than 50% of the intensity of the line is due to Fe XIV (see Fig. 6 in Del Zanna 2012a), hence we identify the 7–376 with the 59.59 Å line.

The second strongest transition is the 20–439 $3s^2\ 3p\ 3d\ ^3P_1$–$3s^2\ 3p\ 4f\ ^3F_2$, with a theoretical wavelength of 62.88 Å. There are few lines in the A85 spectrum around the predicted wavelength. The benchmark carried out in Del Zanna (2012a) suggest that one option is that this line is blended with Fe XIII at 62.98 Å, which is in fact listed as blended in A85. Another option is the unidentified line at 63.57 Å, which results in a difference between predicted and observed energy for $3s^2\ 3p\ 4f\ ^3F_2$ of 25 433 cm^{-1}, much closer to the energy difference for the only 4f level (26 751 cm^{-1}), identified by Kastner et al. (1978). We opt for the second choice.

The next strong transitions are two decays from $3s^2\ 3p\ 4p\ ^3P_0$, level 328. We note that transitions from the $3s^2\ 3p\ 4p$ levels were not identified previously. One option would be that the 7–328 transition is the line observed by A85 at 65.60 Å. Acton et al. identified this line as being due to Mg IX, however, the benchmark carried out in Del Zanna (2012a) indicates that Mg IX should be weak. This identification is excluded because the other decay (the 20–328) would then be expected at 77.28 Å, where A85 does not list any lines. We tentatively identify the 7–328 transition with the unidentified line observed by A85 at 65.90 Å, which would predict the other decay (20–328) at 77.70 Å. There is indeed a line at 77.73 Å listed by A85 as blended. The listed intensity is, however, in agreement with the predicted intensity from a Mg IX line (Del Zanna 2012a). We assume that the intensity provided by A85 refers to the main transition (Mg IX), and does not include the weaker Ni XV line. With this tentative identification, the difference between observed and predicted energy for the $3s^2\ 3p\ 4p\ ^3P_0$ level is 14 668 cm^{-1}, in close agreement with the energy difference for the well-established $3s^2\ 3p\ 4s$ levels. Further measurements, preferably in the laboratory, will be needed to confirm or rule out these tentative identifications.

Finally, comparing the intensities of the soft X-ray lines we have obtained with those obtained with the DW calculations (see Table 3), we can see quite a good agreement for those originating from the $3s^2\ 3p\ 4p$, $3s^2\ 3p\ 4d$, $3s^2\ 3p\ 4f$ configurations but significant increases for those from $3s^2\ 3p\ 4s$. We have seen similar increases in Fe XIII, which are due to the effect of the resonances (Del Zanna & Storey 2013). For example, Fig. 2 (bottom plot) shows the effective collision strengths to the $3s^2\ 3p\ 4s\ ^3P_1$ level.

4. Conclusions

With the present work we have carried out the first R-matrix calculation for Ni XV. Significant differences with the previous DW calculations of Landi & Bhatia (2012) are found, as expected, for a number of transitions. We have provided a complete set of rates and listed the strongest lines of this ion that are observable in astrophysical plasmas. We have assessed all the previous level and line identifications and suggested a few new ones. Our extended calculations and benchmarks for Fe XIII, and the few comparisons with observations discussed here, suggest that the present calculations are very accurate for lines from the $n = 3$ levels, which allow measurements of electron densities in high-temperature (3 MK) plasmas typical of solar active region cores, and of the nickel abundance.

Acknowledgements. The present work was funded by STFC (UK) through the University of Cambridge DAMTP astrophysics grant, and the University of Strathclyde UK APAP network grant ST/J000892/1.

References

Acton, L. W., Bruner, M. E., Brown, W. A., et al. 1985, ApJ, 291, 865 (A85)
Aly, M. K., Evans, J. W., & Orrall, F. Q. 1962, ApJ, 136, 956
Badnell, N. R. 2011, Comput. Phys. Commun., 182, 1528
Badnell, N. R., & Griffin, D. C. 2001, J. Phys. B At. Mol. Phys., 34, 681
Behring, W. E., Cohen, L., & Feldman, U. 1972, ApJ, 175, 493
Berrington, K. A., Eissner, W. B., & Norrington, P. H. 1995, Comput. Phys. Commun., 92, 290
Burgess, A. 1974, J. Phys. B At. Mol. Phys., 7, L364
Burgess, A., & Tully, J. A. 1992, A&A, 254, 436
Burgess, A., Chidichimo, M. C., & Tully, J. A. 1997, J. Phys. B At. Mol. Phys., 30, 33
Chidichimo, M. C., Badnell, N. R., & Tully, J. A. 2003, A&A, 401, 1177
Del Zanna, G. 2009, A&A, 508, 501
Del Zanna, G. 2011, A&A, 533, A12
Del Zanna, G. 2012a, A&A, 546, A97
Del Zanna, G. 2012b, A&A, 537, A38
Del Zanna, G. 2013a, A&A, 555, A47
Del Zanna, G. 2013b, A&A, 558, A73
Del Zanna, G., & Storey, P. J. 2013, A&A, 549, A42
Del Zanna, G., Storey, P. J., Badnell, N. R., & Mason, H. E. 2012, A&A, 541, A90
Edlén, B. 1942, Z. Astrophys., 22, 30
Eissner, W., Jones, M., & Nussbaumer, H. 1974, Comput. Phys. Commun., 8, 270
Fawcett, B. C., & Hatter, A. T. 1980, A&A, 84, 78
Fawcett, B. C., & Hayes, R. W. 1972, J. Phys. B At. Mol. Phys., 5, 366
Fawcett, B. C., Cowan, R. D., & Hayes, R. W. 1972, J. Phys. B At. Mol. Phys., 5, 2143
Feldman, U., Curdt, W., Doschek, G. A., et al. 1998, ApJ, 503, 467
Fisher, R., & Pope, T. 1971, Sol. Phys., 20, 389
Griffin, D. C., Badnell, N. R., & Pindzola, M. S. 1998, J. Phys. B At. Mol. Phys., 31, 3713
Gu, M. F. 2004, in AIP Conf. Ser. 730, eds. J. S. Cohen, D. P. Kilcrease, & S. Mazavet, 127
Hummer, D. G., Berrington, K. A., Eissner, W., et al. 1993, A&A, 279, 298
Jefferies, J. T., Orrall, F. Q., & Zirker, J. B. 1971, Sol. Phys., 16, 103
Kastner, S. O., Swartz, M., Bhatia, A. K., & Lapides, J. 1978, J. Opt. Soc. Am., 68, 1558
Kramida, A., Ralchenko, Y., & Reader, J. 2013, NIST Atomic Spectra Database (ver. 5.1), available at http://physics.nist.gov/asd
Landi, E., & Bhatia, A. K. 2012, At. Data Nucl. Data Tables, 98, 862
Mason, H. E. 1973, Ph.D. Thesis, University of London, UK
Storey, P. J., & Zeippen, C. J. 2010, A&A, 511, A78
Trigueiros, A. G., Borges, F. O., Cavalcanti, G. H., & Farias, E. E. 2006, J. Quant. Spectr. Rad. Transf., 97, 29